Journal Name

ARTICLE TYPE

Template-free Solvothermal Synthesis of WO₃/WO₃·H₂O Hollow Spheres and Their Enhanced Photocatalytic Activity from the Mixture Phase Effect

Yang Liu,[a]Qi Li,*[a]Shian Gao,[a]and Jian Ku Shang[a,b]

Well-defined $WO_3 \cdot H_2O$ hollow spheres composed of nanoflakes were successfully synthesized by a template-free solvothermal process with the i-PrOH/H_2O mixture solvent. In this process, tungsten precursor was firstly hydrolyzed to form solid spheres composed of both $WO_3 \cdot 2H_2O$ and $WO_3 \cdot H_2O$ [10] phases. Then, these solid spheres underwent Ostwald ripening process and the $WO_3 \cdot 2H_2O$ phase was dehydrated to $WO_3 \cdot H_2O$ at the same time to form hollow spheres with pure $WO_3 \cdot H_2O$ phase. With proper calcination temperature, hollow spheres with WO_3 (major) and $WO_3 \cdot H_2O$ (minor) mixture phases were created. These hollow spheres with WO_3 and $WO_3 \cdot H_2O$ mixture phases demonstrated a largely enhanced photocatalytic activity on RhB degradation under visible light irradiation, compared with either pure [15] $WO_3 \cdot H_2O$ hollow spheres or pure WO_3 hollow spheres, which could be attributed to the matched band structure between WO_3 and $WO_3 \cdot H_2O$ phases. Thus, an effective charge carrier separation could happen between WO_3 and $WO_3 \cdot H_2O$ phases of these hollow spheres under visible light irradiation, which contributed to their observed largely enhanced photoctalytic performance.

Introduction

[20] Inorganic materials with hollow spherical structures attracted much research attention due to their specific void interior and consequently unique physical/chemical properties for various applications, such as active-material encapsulation, drug delivery, micro-reactors, filters, piezoelectric transducers, low dielectric [25] constant substrates and so on.[1-5] Many research efforts had been devoted to developing synthesis approaches for hollow spherical materials, including both the template and template-free processes.[1-5] In recent years, the template-free process based on Ostwald ripening had been proved to be an effective approach for [30] the creation of hollow spherical inorganic materials without the potential contamination from templates, and series of hollow spherical inorganic materials had been successfully synthesized through this process, such as TiO_2, Cu_2O, Co_3O_4, ZnS, MnO_2, SnO_2, Fe_3O_4, VO_2, $BaZrO_3$, and so on.[6-13]

[35] As *n*-type semiconductors, tungsten oxide (WO_3) and tungsten oxide hydrates ($WO_3 \cdot nH_2O$) had attracted considerable attention for their applications in gas sensors, electrochromic devices, optical recording devices, and as well as visible-light-responsive photocatalysts.[14] $WO_3 \cdot nH_2O$ was usually synthesized through the [40] liquid-phase synthesis routes, and WO_3 was synthesized by the annealing of $WO_3 \cdot nH_2O$ to remove crystal water. To create WO_3 hollow spheres, $WO_3 \cdot nH_2O$ hollow spheres had been synthesized by both the template process with various sacrificial templates[15-18] and the template-free process via Ostwald ripening.[19-21] But till [45] now, the reported approaches to synthesize $WO_3 \cdot nH_2O$ hollow

spheres by the template-free process were still quite limited in literature, while these previous reports[19-21] had demonstrated that various tungsten precursors and specific synthesis conditions could produce products with different morphologies and crystal [50] structures. Hollow spheres as photocatalysts were beneficial for their photocatalytic performance because the multiple reflections (scattering) from their specific hollow structure could result in a better light harvest and the subsequent generation of more photoelectron-hole pairs.[22-26] Thus, the synthesis of $WO_3 \cdot nH_2O$ [55] hollow spheres via template-free Ostwald ripening mechanism should be further investigated. Recently, we developed a template-free process which successfully synthesized well-dispersed hollow TiO_2 spheres via Ostwald ripening, in which the use of the PrOH/H_2O mixture solvent was critical to create TiO_2 [60] hollow spheres with uniform size and good dispersity.[22] It would be of interest to examine if the PrOH/H_2O mixture solvent could be applicable to synthesize well-defined $WO_3 \cdot nH_2O$ hollow spheres.

For semiconductor photocatalysts, the electron-hole pair [65] recombination problem could cause the loss of a large portion of photo-generated electron-hole pairs, thus reducing their photocatalytic efficiency. Besides noble metal deposition and semiconductor coupling,[27,28] the formation of photocatalysts with mixture phases had also been reported to be beneficial for the [70] separation of electron-hole pairs if these mixture phases had matched band structures.[29-38] For example, enhanced photocatalytic performances had been demonstrated in TiO_2 photocatalysts with mixture phases, including anatase/rutile,[29-32] anatase/brookite,[33,34] anatase/TiO_2(B),[35] and rutile/brookite.[36]

Recently, $In_2O_3/In_2O_3\cdot3H_2O$[37] and $WO_3/WO_3\cdot H_2O$[38] mixture phase photocatalysts were also reported. However, no report is available for the creation of WO_3-based hollow spheres with mixture phases, while the synthesis of WO_3 hollow spheres by the dehydration of $WO_3\cdot nH_2O$ hollow spheres could provide the possibility to create hollow spheres with mixture phases of pure WO_3 and WO_3 with certain amounts of crystal water.

Herein, well-defined $WO_3\cdot H_2O$ hollow spheres composed of nanoflakes were successfully synthesized by a solvothermal process with the i-PrOH/H_2O mixture solvent. Their hollowing process was investigated, which demonstrated clearly that their formation followed Ostwald ripening mechanism. Hollow spheres with WO_3 (major) and $WO_3\cdot H_2O$ (minor) mixture phases were created by calcination with proper temperature, which demonstrated a largely enhanced photocatalytic activity on RhB degradation under visible light irradiation, compared with either pure $WO_3\cdot H_2O$ hollow spheres or pure WO_3 hollow spheres. The $WO_3\cdot H_2O$ phase and WO_3 phase had matched band structure. Thus, an effective charge carrier separation could happen between the WO_3 phase and the $WO_3\cdot H_2O$ phases under visible light irradiation, which contributed to their largely enhanced photoctalytic performance.

Experimental

Chemical and materials

Sodium tungstate dehydrate ($Na_2WO_4\cdot2H_2O$, 99.5%), oxalic acid ($H_2C_2O_4\cdot2H_2O$, 99.8%), hydrochloric acid (HCl, 36%), and isopropyl alcohol (i-PrOH, 99.7%) were purchased from Sinopharm Chemical Reagent Co., Ltd. (Shanghai, P. R. China). Deionized (DI) water was prepared from a lab ultra-pure water purifier. Rhodamine B (RhB, AR) was purchased from Shenyang No. 3 Chemical Reagent Factory (Shenyang, P. R. China).

Template-free synthesis of $WO_3\cdot H_2O$ hollow spheres and their dehydration

$WO_3\cdot H_2O$ hollow spheres were synthesized through a solvothermal process. Under vigorous stirring, 0.5 mmol $Na_2WO_4\cdot2H_2O$ and 1 mmol $H_2C_2O_4\cdot2H_2O$ were added into 30 mL DI water. After they were dissolved completely, 36 mL i-PrOH and 2 mL HCl were added into this aqueous solution in sequence to change the solvent from pure water to an i-PrOH/H_2O mixture. The solution was then transferred into a Teflon-lined autoclave of 90 mL capacity, which was then sealed, kept in an oven at $80\,^{\circ}C$ for 12 h, and air cooled to room temperature afterwards. To obtain samples of various solvothermal reaction times, the autoclave was kept at $80\,^{\circ}C$ for desired time and then water cooled to better reserve the morphology and structure of these samples. The obtained precipitate was centrifuged, washed with water and ethanol for several times, and then dried at $70\,^{\circ}C$ to obtain $WO_3\cdot H_2O$ hollow spheres. $WO_3\cdot H_2O$ hollow spheres were further calcinated at desired temperatures ($200\,^{\circ}C$, $350\,^{\circ}C$, and $500\,^{\circ}C$, respectively) for 2 h in a muffle furnace with a heating rate of $2\,^{\circ}C$/min.

Characterization of hollow spheres

SEM images were obtained on a Leo-Supra-55 scanning electron microscope (Carl Zeiss, Oberkochen, Germany). TEM images and SAED patterns were taken on a JEOL-2100 transmission electron microscope (JEOL, Tokyo, Japan). XRD analysis was conducted on a D/MAX-2004 X-ray powder diffractometer (Rigaku, Tokyo, Japan) with Ni-filtered Cu Kα radiation (0.15418 nm) radiation at 56 kV and 182 mA. TG-DSC curves were measured on a STA-449-C-Jupiter simultaneous thermal analyzer (Netzsch, Selb, Germany) from room temperature to 550 $^{\circ}C$ with a heating rate of 10 $^{\circ}C$/min. The Brunauer-Emmett-Teller (BET) data was measured by nitrogen adsorption-desorption isotherms on an Autosorb-1 surface area and pore size analyzers (Quantachrome, Boynton Beach, USA). The total pore volume and average pore size were derived from the Barrett-Joyner-Halenda (BJH) model. The optical absorbance was determined from the diffuse reflectance spectra (DRS) measurements on a UV-2550 UV-vis spectrophotometer (Shimadzu, Kyoto, Japan) using $BaSO_4$ as the reference.

Photocatalytic degradation of Rhodamine B under visible light irradiation

The photocatalytic performances of both uncalcined and calcined samples were evaluated by their photocatalytic degradation of RhB under visible light irradiation. 50 mg photocatalyst was added into 50 mL RhB solution (20 mg/L) in a 250 mL capacity glass reactor with a quartz top cover. The solution was stirred for 30 min in dark and then exposed to visible light irradiation. The light source was a 300 W Xe arc lamp (PLS-SXE300, Beijing Trusttech Co. Ltd) with a UV cutoff filter ($\lambda > 400$ nm). The light intensity was ~ 100 mW/cm^2. The solution was sampling 2 mL for each time and the concentration of RhB was determined by a UV-vis spectrophotometer (UV-2550, Shimadzu, Kyoto, Japan).

Results and Discussion

The structure and morphology of $WO_3\cdot H_2O$ hollow spheres

Fig. 1 shows the XRD pattern of samples synthesized by a solvothermal process at 80 $^{\circ}C$ for 12 h in the i-PrOH/H_2O mixture solvent. All the diffraction peaks could be indexed as the orthorhombic structure of $WO_3\cdot H_2O$ phase (JCPDS no. 84-0886, space group: Pmnb(62), RIR: 12.81), which suggested that the synthesis process we developed could produce a single phase $WO_3\cdot H_2O$ product. Fig. 2 shows SEM images, TEM images and corresponding SAED patterns of these $WO_3\cdot H_2O$ hollow spheres. It could be observed from the lower magnification SEM image in Fig. 2a that well-defined $WO_3\cdot H_2O$ hollow spheres were successfully created in our approach. Their size is highly uniform with an outer diameter of approximately 2 μm. Fig. 2b shows the higher magnification SEM image of a single hollow sphere, which was enlarged from the one at the center area of Fig. 2a. From its broken shell, the hollow interiors of these spheres could be clearly identified. The shell thickness was ca. 200 nm, and the shell was composed of nanoflakes with the side length from tens to hundreds of nanometers and the thickness from several to tens of nanometers. Furthermore, nanoflakes of smaller size were located at the inner area (as A marked) of the shell, while nanoflakes of larger size were located at the outer area (as B marked) of the shell. This observation indicated a typical Ostwald ripening process, in which smaller crystallites dissolved and were transferred to the outer part for the growth of larger crystallites located at the outer part.[6] Fig. 2c shows the TEM image of a single $WO_3\cdot H_2O$ hollow sphere, in which its hollow nature could

be easily identified from the contrast difference. It could also be observed that these nanoflakes were grown crosswise and large interstices existed between them, which introduced a good permeability to the shells. The permeability nature of the shells could provide an easy access for water, other molecules, and part of the incident photons to the shells and the interior voids. Thus, photocatalytic reactions could happen at either the outer/inner surfaces or the shells of these hollow spheres. Fig. 2d shows its corresponding SAED pattern, which indicated that these hollow spheres had polycrystalline orthorhombic $WO_3 \cdot H_2O$ phase. Fig. 2e shows the TEM image of a single nanoflake, which had a near square shape with approximately 280x200 nm^2 in size. Its corresponding SAED pattern (Fig. 2f) suggested that these nanoflakes had the single crystallinity. The diffraction spots could be indexed as (002) and (200) with the electron beam parallel to the [020] direction. The SAED patterns were in accordance with the XRD analysis result.
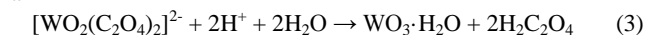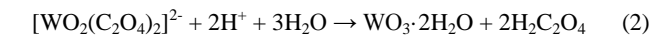
The formation process and mechanism of WO₃·H₂O hollow spheres

To investigate the formation process and mechanism of these hollow $WO_3 \cdot H_2O$ spheres, time-dependent experiments were conducted at 80 ^{o}C with different reaction times. Water cooling was adapted to stop the reaction immediately at desired time to better reserve the morphology and structure of these samples. Fig. 3a, 3b, 3c, and 3d show the TEM images of the time-dependent samples with reaction time of 90, 120, 150, and 180 min, respectively. Fig. 3 demonstrated that the hollow spheres were evolved from the hollowing of solid spheres. Small voids firstly formed at the center of solid spheres, and gradually enlarged to finally form hollow interiors. Fig. 4 shows the XRD patterns of these time-dependent samples accordingly. Different from the pure $WO_3 \cdot H_2O$ phase of the sample with 12 h reaction time (Fig.1), these time-dependent samples (reaction time up to 6 h) were all composed of both the $WO_3 \cdot H_2O$ phase (JCPDS no. 84-0886) and the $WO_3 \cdot 2H_2O$ phase (JCPDS no. 18-1420), and the $WO_3 \cdot H_2O$ phase was the major one. With the reaction time increased from 30 min to 360 min, the diffraction peak strength of the samples increased, indicating the enhanced crystallinity. Meanwhile, for each sample, the relative diffraction peak strength of the $WO_3 \cdot 2H_2O$ phase became weaker and weaker compared with that of the $WO_3 \cdot H_2O$ phase, indicating a phase transition from $WO_3 \cdot 2H_2O$ to $WO_3 \cdot H_2O$ happened with the reaction time increase. After 6 h reaction, only a very small fraction of $WO_3 \cdot 2H_2O$ still existed. After 12 h reaction, the sample had a pure $WO_3 \cdot H_2O$ phase.

Thus, the synthesis of $WO_3 \cdot H_2O$ hollow spheres followed the Ostwald repining mechanism. In this process, $H_2C_2O_4$ and WO_4^{2-} firstly formed the complex ion $[WO_2(C_2O_4)_2]^{2-}$ following Eq. (1):

$$WO_4^{2-} + 2H_2C_2O_4 \rightarrow [WO_2(C_2O_4)_2]^{2-} + 2H_2O \quad (1)$$

It was rather stable and wouldn't react with HCl at room temperature. This step was critical for the creation of the hollow sphere structure. When no $H_2C_2O_4$ was present, precipitates occurred immediately when HCl was added into the sodium tungstate solution, and the final product after solvothermal treatment was composed of irregularly shaped, micrometer-sized crystals.

At elevated temperature under solvothermal conditions, $[WO_2(C_2O_4)_2]^{2-}$ reacted with HCl to form precipitates of both $WO_3 \cdot 2H_2O$ and $WO_3 \cdot H_2O$ with a much slower hydrolysis rate following Eq. (2) and Eq. (3), respectively:

$$[WO_2(C_2O_4)_2]^{2-} + 2H^+ + 3H_2O \rightarrow WO_3 \cdot 2H_2O + 2H_2C_2O_4 \quad (2)$$

$$[WO_2(C_2O_4)_2]^{2-} + 2H^+ + 2H_2O \rightarrow WO_3 \cdot H_2O + 2H_2C_2O_4 \quad (3)$$

These primary crystallites first aggregated into solid spheres as demonstrated in Fig. 3a. Then, these solid spheres underwent the Ostwald ripening to finally form the hollow sphere structure. In the meantime, the phase transition from $WO_3 \cdot 2H_2O$ to $WO_3 \cdot H_2O$ happened following Eq. (4):

$$WO_3 \cdot 2H_2O \rightarrow WO_3 \cdot H_2O + H_2O \quad (4)$$
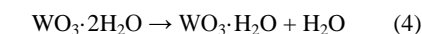
Thus, the amount of $WO_3 \cdot 2H_2O$ gradually decreased with the reaction time increase and it finally disappeared after 12 h reaction due to this dehydration reaction.

In this approach, another critical factor for the formation of well-defined hollow $WO_3 \cdot H_2O$ spheres was the use of i-PrOH/H_2O mixture solvent. When only water was used as the solvent, the obtained product was composed of both individual nanoflakes and hollow spherical aggregates from nanoflakes with different sizes and shapes (see Fig. S1 in the Electronic Supplementary Information). As we found for n-PrOH in the creation of well-dispersed hollow TiO_2 spheres in our previous work,[22] the introduction of i-PrOH to H_2O could reduce the hydrolysis rate of tungsten precursor, which was beneficial for the primary crystallites to aggregate into well-defined solid spheres.

The creation of hollow spheres with WO₃·H₂O and WO₃ mixture phases

Thermal analysis was conducted on the $WO_3 \cdot H_2O$ hollow sphere sample by measuring its TG and DSC curves as demonstrated in Fig. 5a. The sample was heated from room temperature to 550 ^{o}C with a heating rate of 10 ^{o}C/min, and then cooled to room temperature. From room temperature to ~ 170 ^{o}C, the TG curve showed a slight decrease of ca. 0.7% and a broad weak endothermic peak occurred on the corresponding DSC curve. This part of mass loss mainly came from the evaporation of surface adsorbed water. From ~ 170 ^{o}C to ~ 280 ^{o}C, the TG curve had a large decrease of ca. 6.7%, and a large endothermic peak occurred on the corresponding DSC curve with the peak position at ~ 218 ^{o}C. From ~ 280 ^{o}C to ~ 500 ^{o}C, the TG curve had a slight decrease of ca. 0.3%, and the DSC curve showed a continuous endothermic process. Thus, the sum of these two parts of mass loss of ca. 7% came from the phase transition from $WO_3 \cdot H_2O$ to WO_3. The theoretical mass loss in the process is 7.2%, very close to the experimental data. Thermal analysis suggested that the phase transition from $WO_3 \cdot H_2O$ to WO_3 began at ~ 170 ^{o}C and mostly finished at ~ 280 ^{o}C. With further temperature increase, the residual crystal water was removed and the crystallinity of WO_3 enhanced.

From the thermal analysis result, three temperatures of 200, 350 and 500 ^{o}C were chosen for the calcination of as prepared $WO_3 \cdot H_2O$ hollow spheres, respectively, to create final products

with different phases. Fig. 5b shows the XRD patterns of these three samples calcined at different temperatures. The as prepared $WO_3 \cdot H_2O$ hollow spheres had the pure orthorhombic $WO_3 \cdot H_2O$ phase. After calcination at 500 °C for 2 h, the sample completely
5 conversed to well-crystallized, pure WO_3 phase (JCPDS no. 43-1035, space group: P21/n(14), RIR: 5.04) with three distinct strong diffraction peaks of (002), (020), and (200). The sample calcined at 350 °C also only had the pure WO_3 phase, while the intensity of its diffraction peaks was weaker. In the XRD pattern
10 of the sample calcined at 200 °C, however, two sets of diffraction peaks could be identified. Besides the major phase of WO_3, the (111) and (020) diffraction peaks of $WO_3 \cdot H_2O$ could also be observed, which suggested that it was composed of a mixture of WO_3 and $WO_3 \cdot H_2O$. The $WO_3/WO_3 \cdot H_2O$ weight ratio (ω_1/ω_2) in
15 the sample calcined at 200 °C could be estimated by the reference intensity method using following Eq. (5):

$$\frac{I_1}{I_2} = \frac{RIR_1}{RIR_2} \frac{\omega_1}{\omega_2} \qquad (5)$$

20 where I_1 and I_2 are the intensities of WO_3 (200) peak and $WO_3 \cdot H_2O$ (111) peak, respectively, measured from the XRD pattern. RIR_1 and RIR_2 are the reference intensities of the WO_3 and $WO_3 \cdot H_2O$ phase compared to α-Al_2O_3 standard, respectively, got from the JCPDS cards. And its boundary condition is that the
25 sum of ω_1 and ω_2 is 1. From the XRD data, it could be roughly estimated that ω_1/ω_2 was ~ 0.91/0.09. Thus, the calcination temperature of 200 °C chosen based on the thermal analysis result created the final product with the $WO_3/WO_3 \cdot H_2O$ mixture phases.

Fig. 5c shows the SEM image of the sample calcined at 200
30 °C, and SEM images of samples calcined at 350 °C and 500 °C could be found in Fig. S2 in the Electronic Supplementary Information. After calcination, all samples kept their hollow sphere morphology, which indicated that the mechanical strength of these hollow spheres was pretty good during the calcination to
35 sustain their structure. Similar observations had been reported on $WO_3 \cdot nH_2O$ hollow structures[17,18,21] and TiO_2 hollow structures[22,23], in which hollow structures were well maintained during the calcination process.

Table 1 summarizes the data of BET specific surface area, pore
40 volume, and pore size for these samples. The sample calcined at 200 °C had very close BET specific surface area, pore volume, and pore size with the as prepared $WO_3 \cdot H_2O$ hollow spheres. When the calcination temperature increased to 350 °C and 500 °C, the obtained sample's BET specific surface area decreased ~
45 20% and ~ 58%, respectively, and their pore volume and pore size also decreased. These results were in accordance with the XRD and DSC analysis results. With a higher calcination temperature, the sample's crystallinity increases, this induces a lower BET specific surface area and smaller pore size/volume.
50 Similar results had been reported in the calcination of $WO_3 \cdot H_2O$ hollow spheres.[18]

Optical properties of hollow sphere samples

The optical absorbance of these samples was investigated by UV-vis diffuse reflectance spectra (DRS) measurement, as shown in
55 Fig. 6a. From the reflectance data, optical absorbance could be approximated by the Kubelka-Munk function, as given by Eq. (6):

$$F(R) = \frac{(1-R)^2}{2R} \qquad (6)$$

60 where R is the diffuse reflectance.[39] The as prepared $WO_3 \cdot H_2O$ hollow spheres had an absorption edge at ~ 525 nm, indicating a good visible light absorption capability. After calcination, the absorption stopping edges of all samples blue shifted. Samples
65 calcined at 350 °C and 500 °C had very close light absorption curves with the stopping edge at ~ 455 nm, while the sample calcined at 200 °C had a better visible light absorption with the stopping edge at ~ 510 nm. Samples calcined at 350 °C and 500 °C both were composed of pure WO_3 phase so they had almost
70 identical light absorption curves. The sample calcinated at 200 °C, however, was composed of the mixture of both WO_3 (major) and $WO_3 \cdot H_2O$ (minor) phases. Thus, its light absorption curve was between that of WO_3 and $WO_3 \cdot H_2O$, and more close to that of WO_3.

75 For semiconductors, the optical absorption near the band edge follows the Eq. (7):[39]

$$\alpha h v = A(h v - E_g)^n \qquad (7)$$

80 where α, v, A, and E_g are the absorption coefficient, light frequency, proportionality constant, and band gap, respectively, and n equals either 0.5 for allowed direct transition or 2 for allowed indirect transition. The optical band gap of tungsten oxide (hydrate) is between the oxygen 2p orbitals and tungsten 5d
85 orbitals, and they are indirect band transitions.[40,41] So the value of n is determined as 2. Fig. 6b shows the Tauc Plots (($\alpha h v$)$^{1/2}$ vs. $h v$) of the as prepared $WO_3 \cdot H_2O$ hollow spheres and the sample calcined at 500 °C (pure WO_3 phase) constructed from Fig. 6a, respectively, which demonstrated the linear Tauc Region just
90 above the optical absorption edge to determine the semiconductor band gap. Extrapolation of this line to the photon energy axis yields the semiconductor band gap. Thus, the E_g of $WO_3 \cdot H_2O$ was determined to be ~ 2.35 eV, and the E_g of WO_3 was determined to be ~ 2.72 eV.

95 **Photocatalytic degradation of RhB under visible light irradiation by hollow sphere samples**

The photocatalytic activities of these hollow sphere samples were demonstrated by their degradation effect on RhB under visible light irradiation, as shown in Fig. 7. A control experiment with
100 only visible light irradiation was also conducted, and no RhB concentration change was observed which suggested that the visible light irradiation itself could not degrade RhB (not shown in Fig. 7). Before the photocatalytic degradation experiment, all samples were mixed with the RhB solution in the dark to reach
105 the adsorption-desorption equilibrium. It was found that 0.5 h was enough for the adsorption-desorption equilibrium to be established for these samples. For example, the adsorption kinetic curve of the sample calcined at 200 °C was shown in Fig. 7, which demonstrated that the residual RhB concentration reached
110 a plateau after 0.5 h adsorption. The dark adsorption could remove ~ 18%, ~ 18%, ~ 13%, and ~ 8% RhB in the RhB solution for the as prepared $WO_3 \cdot H_2O$ hollow spheres, samples calcined at 200 °C, 350 °C, and 500 °C, respectively. The difference observed may be attributed to their BET specific surface area differences.

When the visible light irradiation was on, all samples demonstrated photocatalytic RhB degradation activities, which could be attributed to their visible light absorption as demonstrated in Fig. 6a. After 5 h visible light irradiation, ~ 24%,
5 ~ 60%, ~ 23%, and ~ 22% RhB in the RhB solution was further removed by the photocatalytic degradation from the as prepared $WO_3 \cdot H_2O$ hollow spheres, and samples calcined at 200 °C, 350 °C, and 500 °C, respectively. Thus, the sample calcined at 200 °C demonstrated the best photocatalytic RhB degradation effect
10 under visible light irradiation among these four hollow sphere samples.

The slope of the RhB degradation curve in Fig. 7 represents the RhB degradation rate at certain treatment time. The photocatalytic activity enhancement could be further
15 demonstrated quantitatively by the initial RhB degradation rates for different photocatalysts. The initial RhB degradation rates were determined at ~ 1.2, ~ 4.4, ~ 1.8, and ~ 1.4 mg/(g·h) for the as prepared $WO_3 \cdot H_2O$ hollow spheres, samples calcined at 200 °C, 350 °C, and 500 °C, respectively. The initial photocatalytic
20 RhB degradation rate by the sample calcined at 200 °C was ~ 3.7, ~ 2.4, ~ 3.1 times of that by the as prepared $WO_3 \cdot H_2O$ hollow spheres, samples calcined at 350 °C, and 500 °C, respectively, which clearly demonstrated its largely enhanced photocatalytic activity under visible light irradiation.

25 **Photocatalytic enhancement mechanism of the $WO_3/WO_3 \cdot H_2O$ sample**

Although the visible light absorption of the as prepared $WO_3 \cdot H_2O$ hollow spheres was stronger than that of the sample calcined at 200 °C and their BET specific surface areas were
30 very close, its photocatalytic RhB degradation performance under visible light illumination was much worse than that of the sample calcined at 200 °C. For pure WO_3 hollow spheres (samples calcined at 350 °C and 500 °C), they had much better crystallinity than that of the sample calcined at 200 °C.
35 However, their initial photocatalytic RhB degradation rates were just ~ 41% and ~ 32% as that of the sample calcined at 200 °C, while their BET specific surface areas were ~ 79% and ~ 42% as that of the sample calcined at 200 °C, respectively. This observation suggested that the surface area difference itself could
40 not explain their different photocatalytic activities.

It is well known that photocatalysts may not demonstrate good photocatalytic activity even with high light absorption because of the loss of charge carriers due to their recombination. The effective separation of charge carriers is critical to their
45 photocatalytic performances. The largely enhanced photocatalytic activity of the sample calcined at 200 °C under visible light irradiation could be attributed to its specific mixture nature of both WO_3 and $WO_3 \cdot H_2O$ phases. The E_g values of $WO_3 \cdot H_2O$ and WO_3 were determined from the Tauc Plots (Fig. 6b) as ~ 2.35 eV
50 and ~ 2.72 eV, respectively. The conduction band (CB) bottom values and valence band (VB) top values of the two semiconductors could be estimated by Eq. (8) and Eq. (9): [42]

$$E_{CB} \approx X_{comp} - E^e - 1/2E_g \quad (8)$$

55

$$E_{VB} = E_{CB} + E_g \quad (9)$$

where E^e equals 4.5 eV and X_{comp} is the electronegativity of a compound. Calculation details could be found in the Electronic
60 Supplementary Information, which demonstrated that the CB and VB edges of WO_3 were ~ 0.73 and ~ 3.45 eV with respect to the NHE, respectively, and the CB and VB edges of $WO_3 \cdot H_2O$ were ~ 1.21 and ~ 3.56 eV with respect to the NHE, respectively. Thus, an effective charge carrier separation could happen between the
65 WO_3 and $WO_3 \cdot H_2O$ phases, as schematically illustrated in Fig. 8.When the sample calcined at 200 °C was exposed to visible light irradiation, both WO_3 and $WO_3 \cdot H_2O$ phases could be exited and subsequently generate electron-hole pairs. Because the CB of WO_3 was more negative than that of $WO_3 \cdot H_2O$, photo-generated
70 electrons at CB of WO_3 could flow to the CB of $WO_3 \cdot H_2O$, while photo-generated holes at VB of $WO_3 \cdot H_2O$ could flow to the VB of WO_3 because the VB of $WO_3 \cdot H_2O$ was more positive than that of WO_3. Thus, photo-generated electrons and holes could be separated effectively from each other and further react with
75 electron acceptors and electron donors, respectively, which contributed to the largely enhanced photoctalytic performance.

Conclusions

In summary, well-defined $WO_3 \cdot H_2O$ hollow spheres composed of nanoflakes were synthesized through a template-free
80 solvothermal process via Ostwald ripening. Hollow spheres with WO_3 (major) and $WO_3 \cdot H_2O$ (minor) mixture phases were created by calcination with proper temperature, and a matched band structure was created between the two phases. Thus, an effective charge carrier separation could happen between the WO_3 phase
85 and the $WO_3 \cdot H_2O$ phases under visible light irradiation, these hollow spheres with WO_3 and $WO_3 \cdot H_2O$ mixture phases demonstrated a largely enhanced photocatalytic activity on RhB degradation under visible light irradiation, compared with either pure $WO_3 \cdot H_2O$ hollow spheres or pure WO_3 hollow spheres.

90 ## Acknowledgements

100 ## Notes and references

[a]Environment Functional Materials Division, Shenyang National Laboratory for Materials Science, Institute of Metal Research, Chinese Academy of Sciences, Shenyang, 110016, P. R. China. Fax: +86-24-23971215; Tel.: +86-24-83978028; E-mail: qili@imr.ac.cn (Q. Li)
105 *[b]Department of Materials Science and Engineering University of Illinois at Urbana-Champaign, Urbana, IL 61801, USA*

† Electronic Supplementary Information (ESI) available: [SEM images of the sample synthesized with DI H_2O only as the solvent, SEM images of
110 the samples calcined at 350 °C and 500 °C, and the estimation of the CB and VB edges of WO_3 and $WO_3 \cdot H_2O$]. See DOI: 10.1039/b000000x/

1   J. K. Cochran, *Curr. Opin. Solid State Mater. Sci.,* 1998, **3**, 474.
2   X. W. Lou, L. A. Archer, Z. Yang, *Adv. Mater.*, 2008, **20**, 3987.

3   Q. Zhang, W. Wang, J. Goebl, Y. Yin, *Nano Today*, 2009, **4**, 494.

4   Y. Zhao, L. Jiang, *Adv. Mater.*, 2009, **21**, 3621.

5   J. Hu, M. Chen, X. Fang, L. Wu, *Chem. Soc. Rev.*, 2011, **40**, 5472.

6   H.G. Yang, H. C. Zeng, *J. Phys. Chem. B*, 2004, **108**, 3492.

7   Y. Chang, J. J. Teo, H. C. Zeng, *Langmuir*, 2005, **21,** 1074.

8   B. Liu, H. C. Zeng, *Small*, 2005, **1,** 566.

9   B. Li, G. Rong, Y. Xie, L. Huang, C. Feng, *Inorg. Chem.*, 2006, **45,** 6404.

10   X. W. Lou, Y. Wang, C. Yuan, J. Y. Lee, L. A. Archer, *Adv. Mater.*, 2006, **18**, 2325.

11   B. Jia, L. Gao, *J. Phys. Chem. C*, 2008, **112**, 666.

12   F. Y. Kong, M. Li, X. Y. Yao, J. M. Xu, A. D. Wang, Z. P. Liu, G. H. Li, *CrystEngComm*, 2012, **14**, 3858.

13   Z. Dong, T. Ye, Y. Zhao, J. Yu, F. Wang, L. Zhang, X. Wang, S. Guo, *J. Mater. Chem.*, 2011, **21**, 5978.

14   H. Zheng, J. Z. Ou, M. S. Strano, R. B. Kaner, A. Mitchell, K. Kalantar-zadeh, *Adv. Funct. Mater.*, 2011, **21**, 2175.

15   X. L. Li, T. J. Lou, X. M. Sun, Y. D. Li, *Inorg. Chem.*, 2004, **43**, 5442.

16   X. Zhao, T. L.Y. Cheung, X. Zhang, D. H. L. Ng, J. Yu, *J. Am. Ceram. Soc.*, 2006, **89**, 2960.

17   D. Chen, J. Ye, *Adv. Funct. Mater.*, 2008, **18**, 1922.

18   J. Yu, L. Qi, B. Cheng, X. Zhao, *J. Hazard. Mater.*, 2008, **160**, 621.

19   S. Jeon, K. Yong, *Chem. Commun.*, 2009, 7042.

20   Z. G. Zhao, M. Miyauchi, *J. Phys. Chem. C*, 2009, **113**, 6539.

21   J. Huang, X. Xu, C. Gu, G. Fu, W. Wang, J. Liu, *Mater. Res. Bull.*, 2012, **47**, 3224.

22   Y. Liu, Q. Li, S. Gao, J. K. Shang, *J. Am. Ceram. Soc.*, 2013, **96**, 1421.

23   H. Li, Z. Bian, J. Zhu, D. Zhang, G. Li, Y. Huo, H. Li, Y. Lu, *J. Am. Chem. Soc.*, 2007, **129**, 8406.

24   Y. Li, T. Kunitake, S. Fujikawa, *J. Phys. Chem. B*, 2006, **110**, 13000.

25   Y. Kondo, H. Yoshikawa, K. Awaga, M. Murayama, T. Mori, K. Sunada, S. Bandow, S. Iijima, *Langmuir*, 2008, **24**, 547.

26   H. J. Koo, Y. J. Kim, Y. H. Lee, W. I. Lee, K. Kim, N. G. Park, *Adv. Mater.* 2008, **20**, 195.

27   H. Zhang, G. Chen, D. W. Bahnemann, *J. Mater. Chem.* 2009, **19,** 5089.

28   S. G. Kumar, L. G. Devi, *J. Phys. Chem. A,* 2011, **115**, 13211.

29   D. C. Hurum, A. G. Agrios, K. A. Gray, T. Rajh, M. C. Thurnauer, *J. Phys. Chem B*, 2003, **107**, 4545.

30   S. Bakardjieva, J. Šubrt, V. Štengl, M. J. Dianez, M. J. Sayagues, *Appl. Catal. B Environ.*, 2005, **58**, 193.

31   B. Sun, P. G. Smirniotis, *Catal. Today*, 2003, **88**, 49

32   T. van der Meulen, A. Mattson, L. Österlund, *J. Catal.*, 2007, **251**, 131.

33   S. Ardizzone, C. L. Bianchi, G. Cappelletti, S. Gialanella, C. Pirola, V. Ragaini, *J. Phys. Chem. C*, 2007, **111**, 13222.

34   T. Ozawa, M. Iwasaki, H. Tada, T. Akita, K. Tanaka, S. Ito, *J. Colloid Interface Sci.*, 2005, **281**, 510.

35   W. Li, C. Liu, Y. Zhou, Y. Bai, X. Feng, Z. Yang, L. Lu, X. Lu, K. Y. Chan, *J. Phys. Chem. C*, 2008, **112**, 20539.

36   H. Xu, L. Zhang, *J. Phys. Chem. C*, 2009, **113**, 1785.

37   S. Chen, X. Yu, H. Zhang, W. Liu, *J. Hazard. Mater.*, 2010, **180**, 735.

38   J. Cao, B. Luo, H. Lin, B. Xu, S. Chen, *Appl. Catal. B Environ.*, 2012, **111-112**, 288.

39   J. Tauc, R. Grigorovici, A. Vancu, *Phys. Stat. Sol.*, 1966, **15**, 627.

40   C. G. Grandqvist, A. Azens, A. Hjelm, L. Kullman, G. A. Niklasson, D. Rönnow, M. Strømme Mattsson, M. Veszelei, G. Vaivars, *Sol. Energy*, 1998, **63**, 199.

41   S. H. Baeck, T. F. Jaramillo, C. Brändli, E. W. McFarland, *J. Comb. Chem.*, 2002, **4**, 536.

42   P. Wang, B. Huang, X. Zhang, X. Qin, Y. Dai, H. Jin, J. Wei, M. H. Whangbo, *Chem. Eur. J.*, 2008, **14**, 10543.

CrystEngComm Accepted Manuscript

Journal Name

CrystEngComm

ARTICLE TYPE

Tables:

Table 1 BET data of the as prepared $WO_3 \cdot H_2O$ hollow spheres, samples calcinated at 200 ^oC, 350 ^oC, and 500 ^oC, respectively.

Sample	Specific surface area (m^2/g)	Total pore volume (cm^3/g)	Average pore size(nm)
$WO_3 \cdot H_2O$	22.0	0.077	15.4
200^oC	22.2	0.079	14.2
350^oC	17.6	0.062	13.8
500^oC	9.3	0.022	9.6

5

Journal Name

CrystEngComm

ARTICLE TYPE

Figure Captions:

Fig. 1 XRD patterns of the as prepared $WO_3 \cdot H_2O$ hollow spheres.

5 Fig. 2 SEM images of the as prepared $WO_3 \cdot H_2O$ hollow spheres with (a) a lower magnification and (b) a higher magnification, respectively. (c) TEM image of a single $WO_3 \cdot H_2O$ hollow sphere. (d) The corresponding SAED pattern of the single $WO_3 \cdot H_2O$ hollow sphere in (c). (e) TEM image of a single nanoflake. (f)
10 The corresponding SAED pattern of the single nanoflake in (e).

Fig. 3 TEM images of the time-dependent samples synthesized at 80 ^{o}C for (a) 90 min, (b) 120 min, (c) 150 min, and (d) 180 min, respectively.

15

Fig. 4 XRD patterns of the time-dependent samples synthesized at 80 ^{o}C for 30 min, 90 min, 180 min, and 360 min, respectively.

Fig. 5 (a) TG-DSC curves of the as prepared $WO_3 \cdot H_2O$ hollow
20 spheres. (b) XRD patterns of samples calcinated at 200 ^{o}C, 350 ^{o}C, and 500 ^{o}C, respectively. (c) SEM image of the sample calcined at 200 ^{o}C.

Fig. 6 (a) Optical absorbance curves of the as prepared $WO_3 \cdot H_2O$
25 hollow spheres, samples calcinated at 200 ^{o}C, 350 ^{o}C, and 500 ^{o}C, respectively. (b) Tauc Plots of the as prepared $WO_3 \cdot H_2O$ spheres and the sample calcinated at 500 ^{o}C (pure WO_3 phase), respectively, constructed from Fig. 6 (a).

30 Fig. 7 Photocatalytic degradation curves of RhB under visible light irradiation by the as prepared $WO_3 \cdot H_2O$ hollow spheres, samples calcinated at 200 ^{o}C, 350 ^{o}C, and 500 ^{o}C, respectively.

Fig. 8 Schematic illustration of the matched band structure and
35 the charge carrier separation in the $WO_3/WO_3 \cdot H_2O$ mixture phase sample under visible light irradiation.

Journal Name

CrystEngComm

ARTICLE TYPE

Table of contents
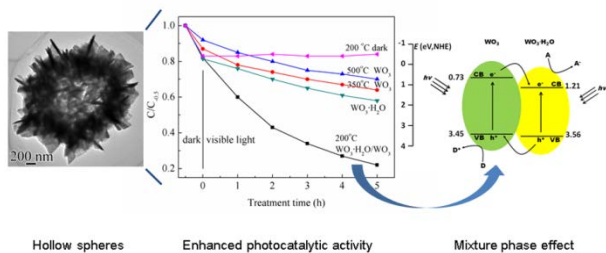
Hollow spheres   Enhanced photocatalytic activity   Mixture phase effect

$WO_3/WO_3 \cdot H_2O$ mixture phase hollow sphere photocatalyst was created through a template-free process, which demonstrated
5 enhanced visible light photocatalytic activity.
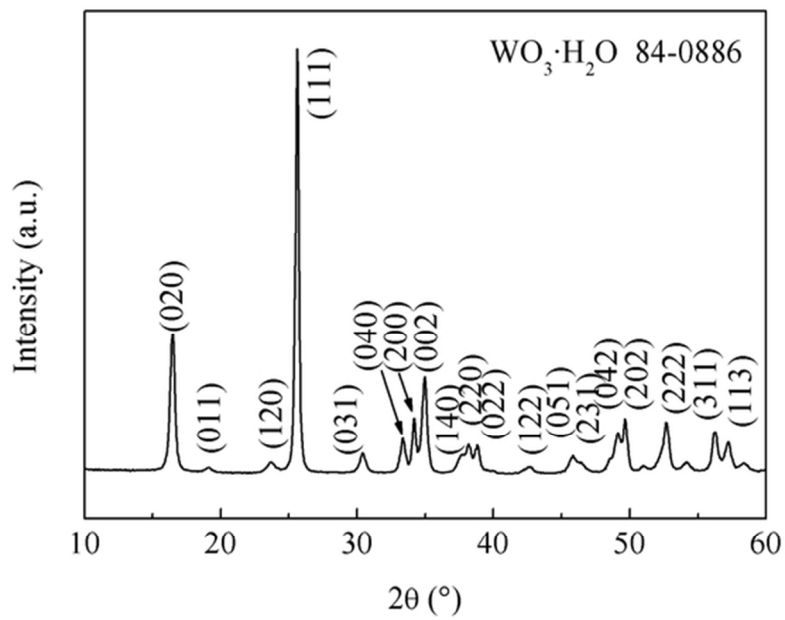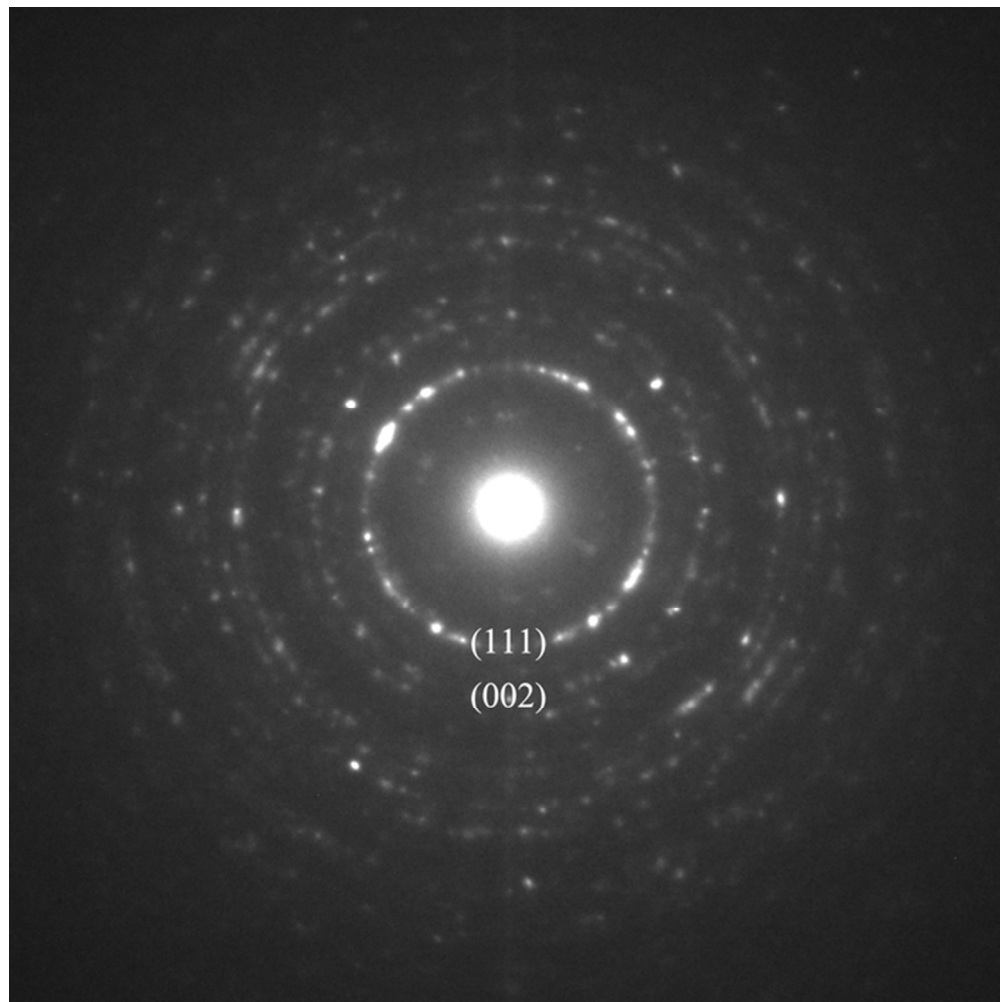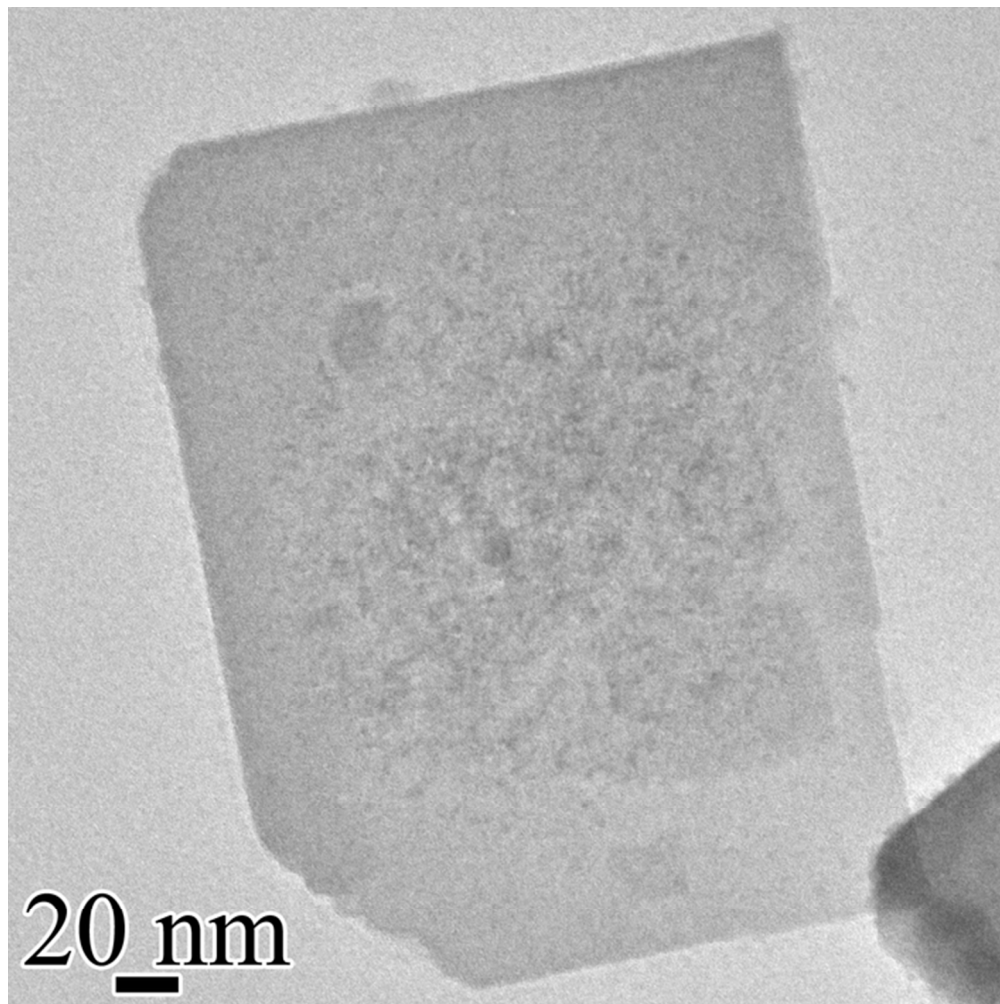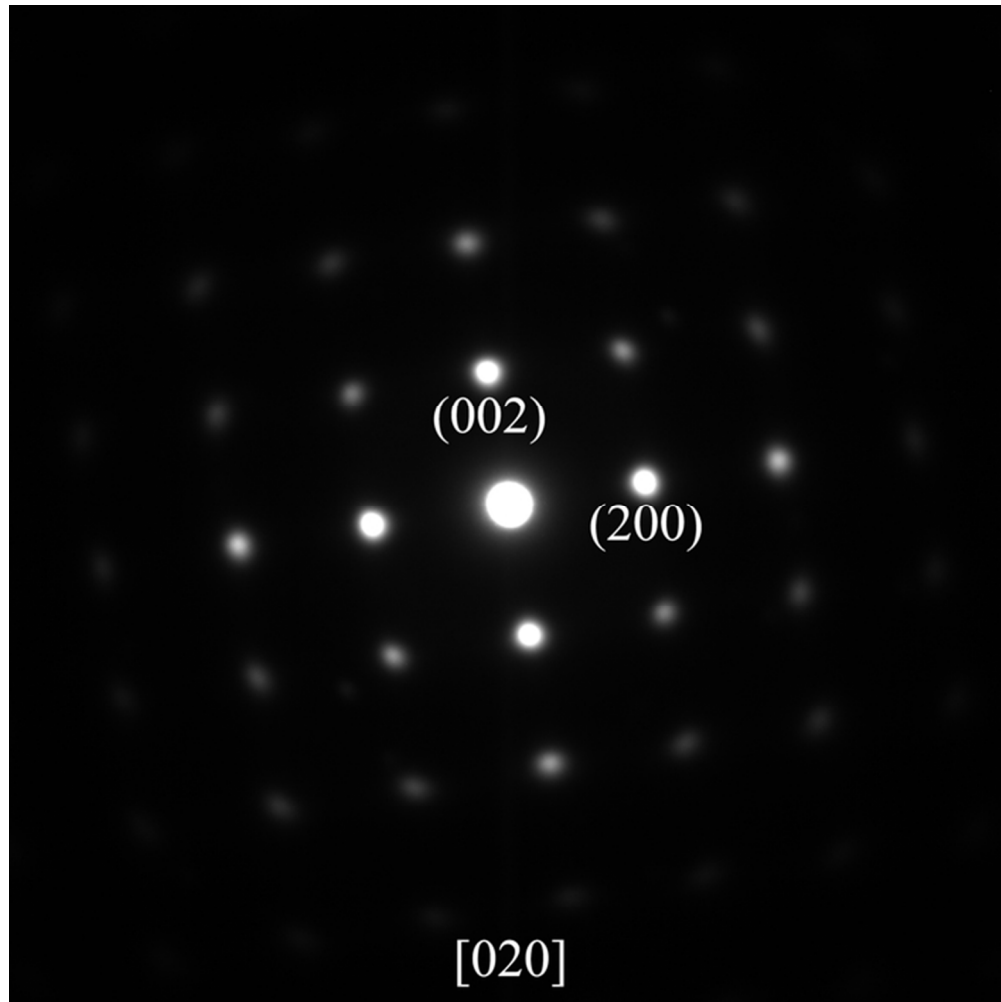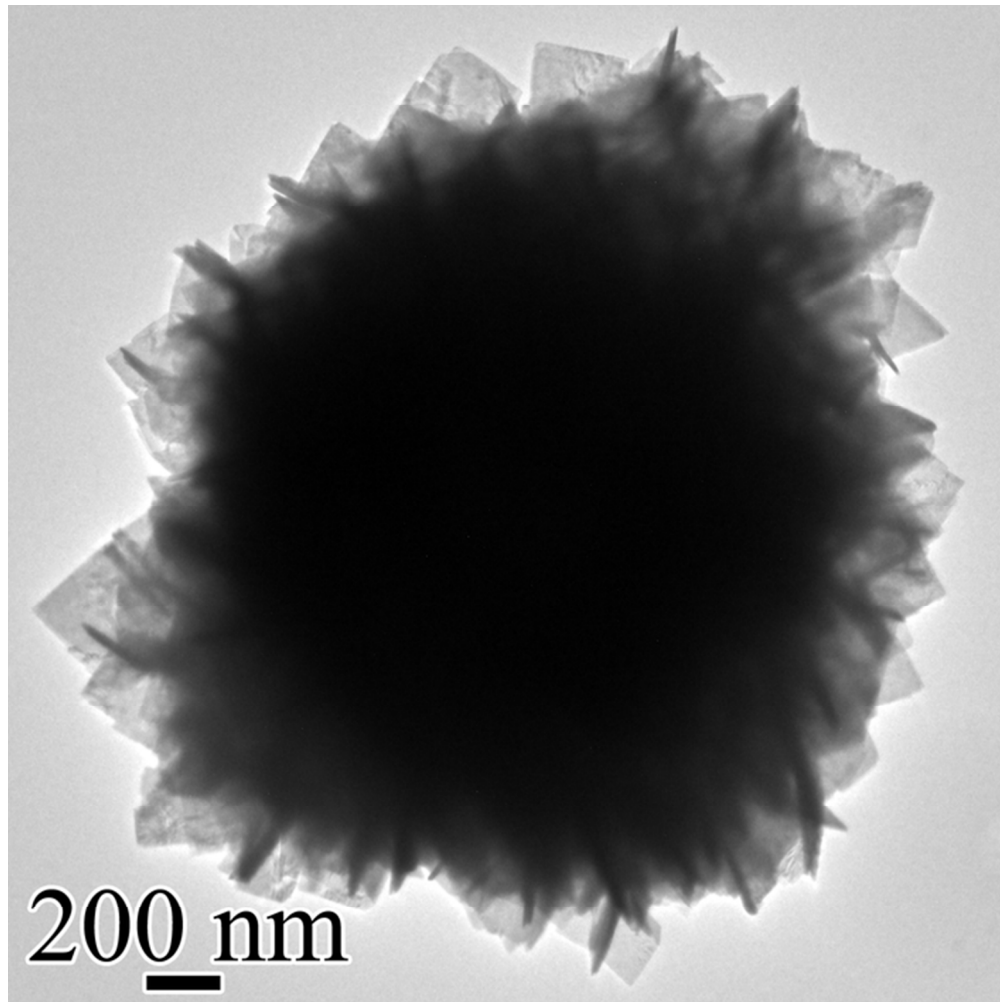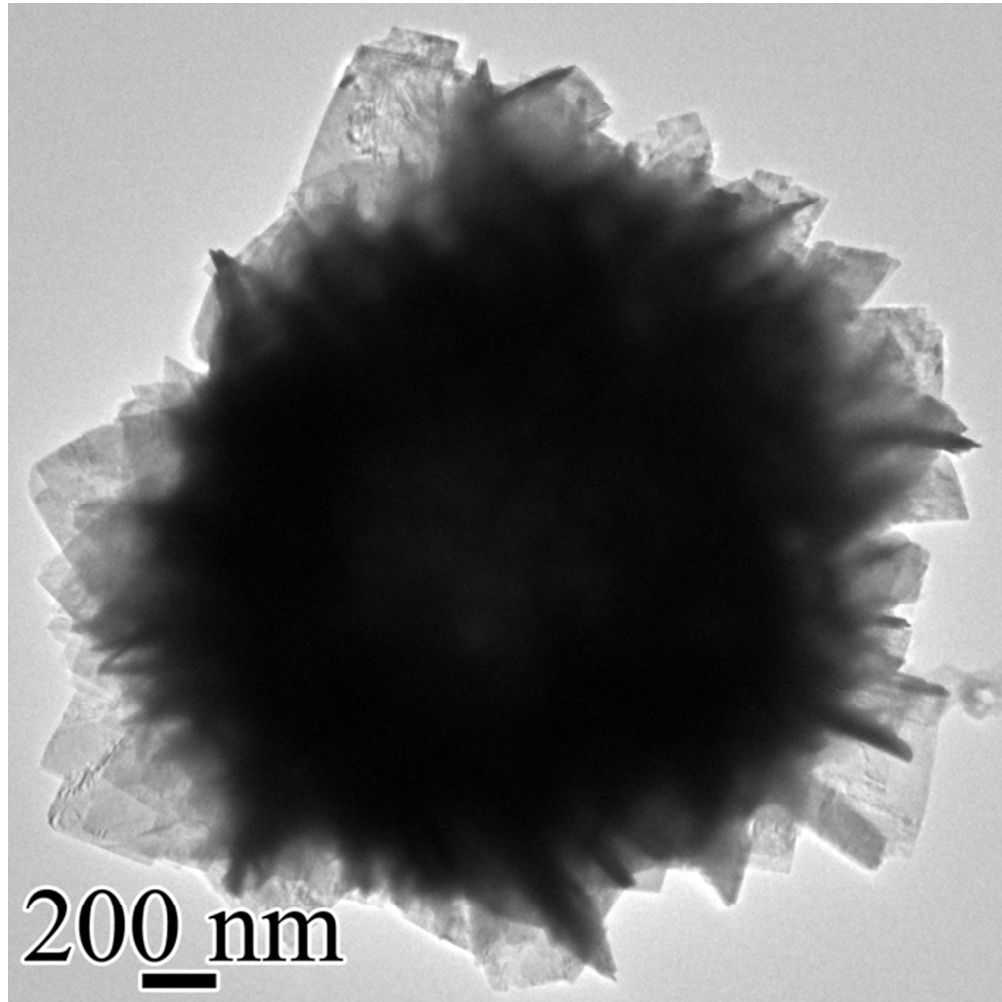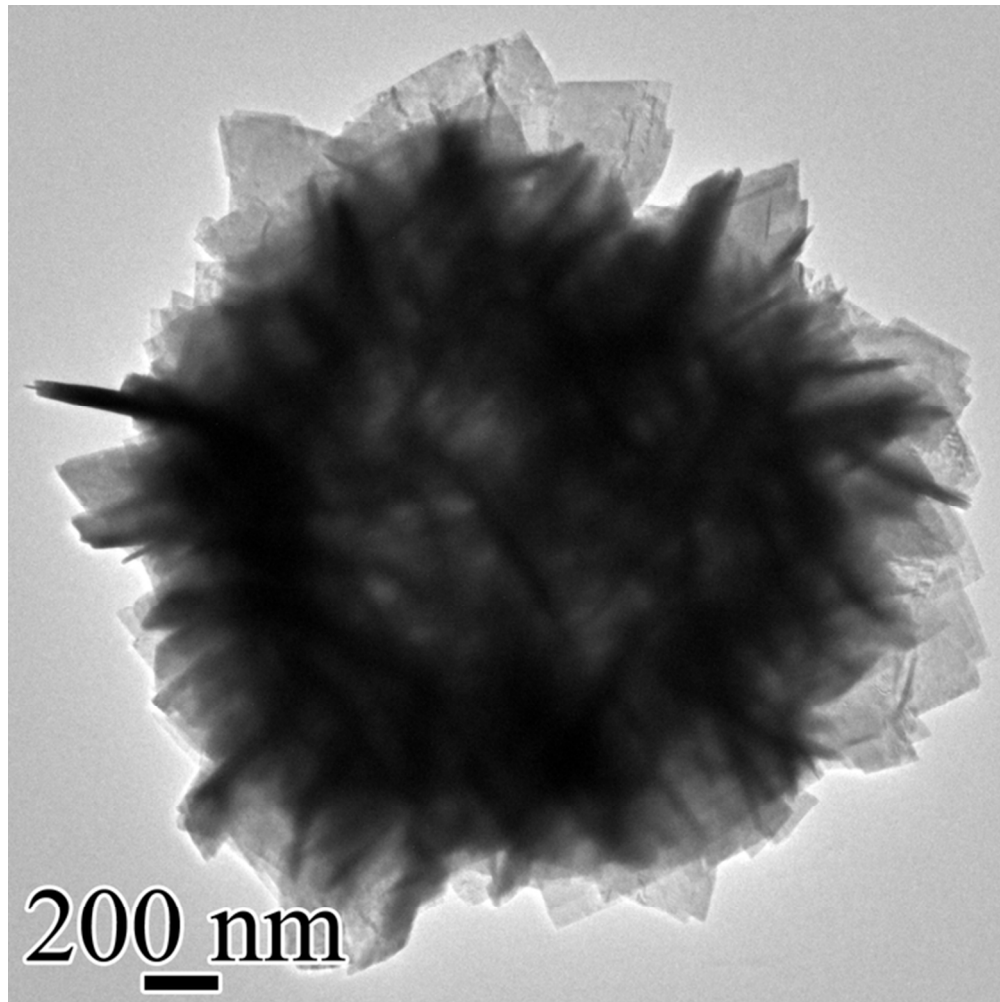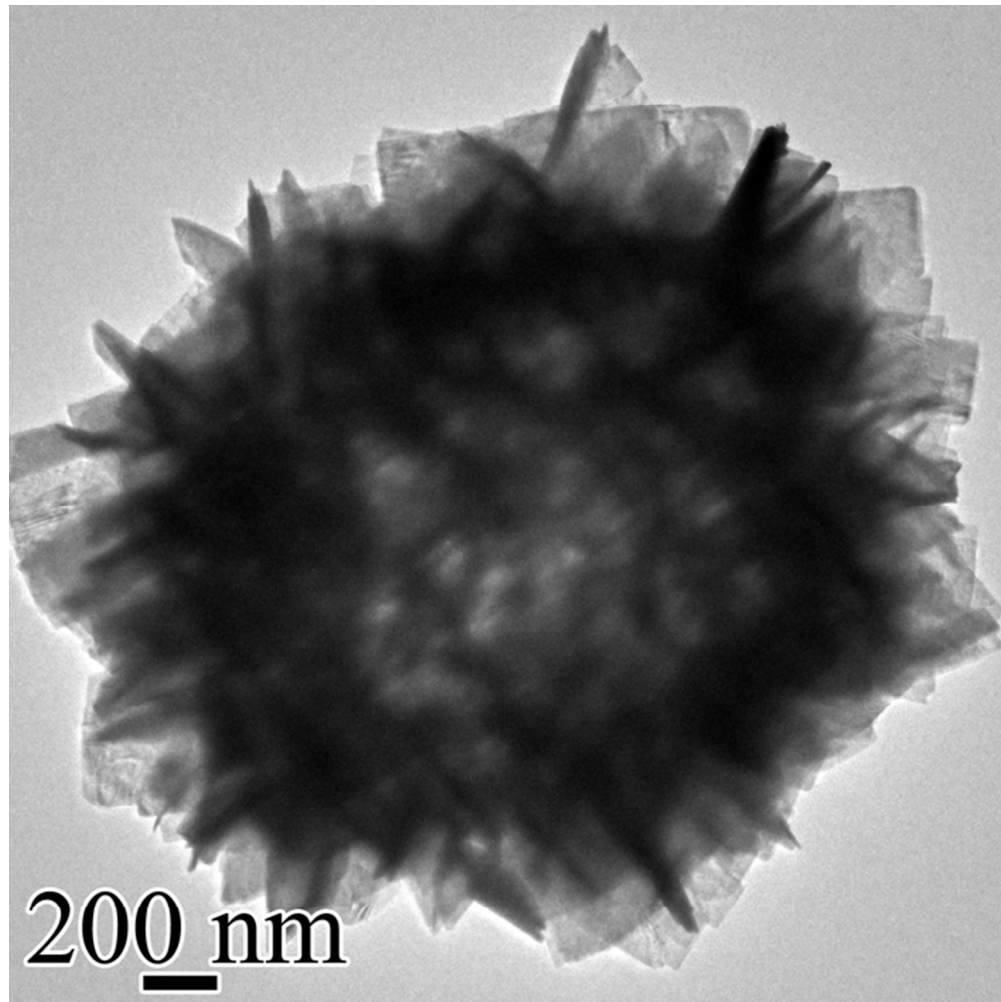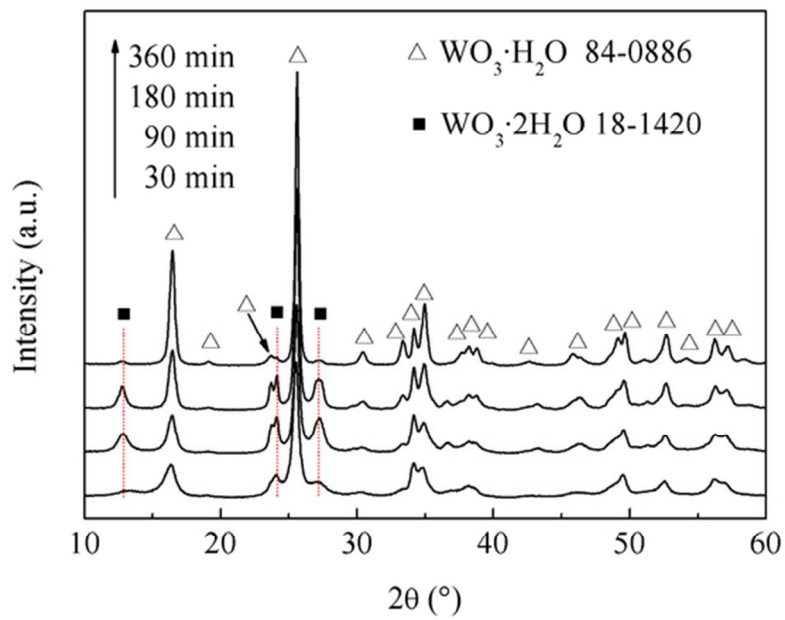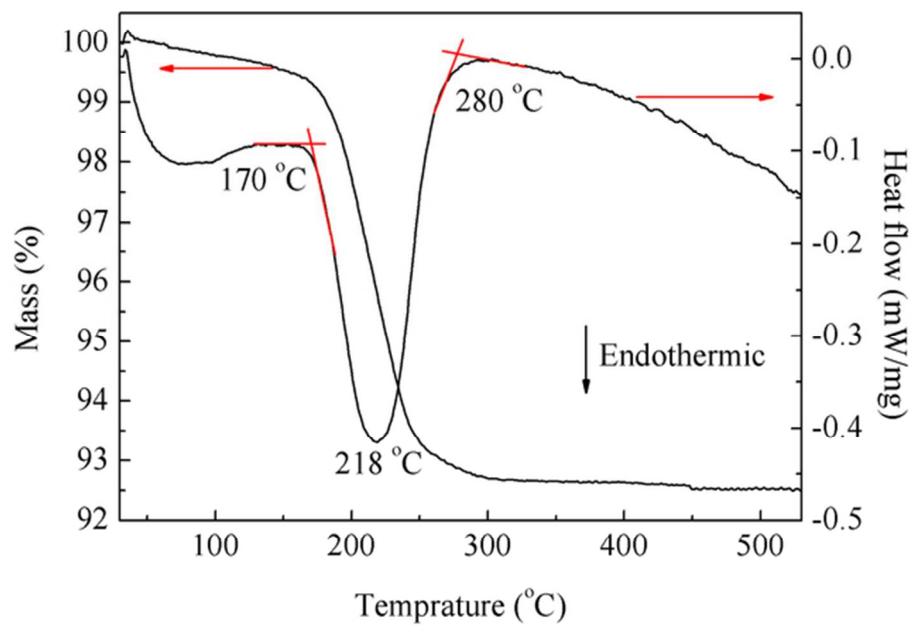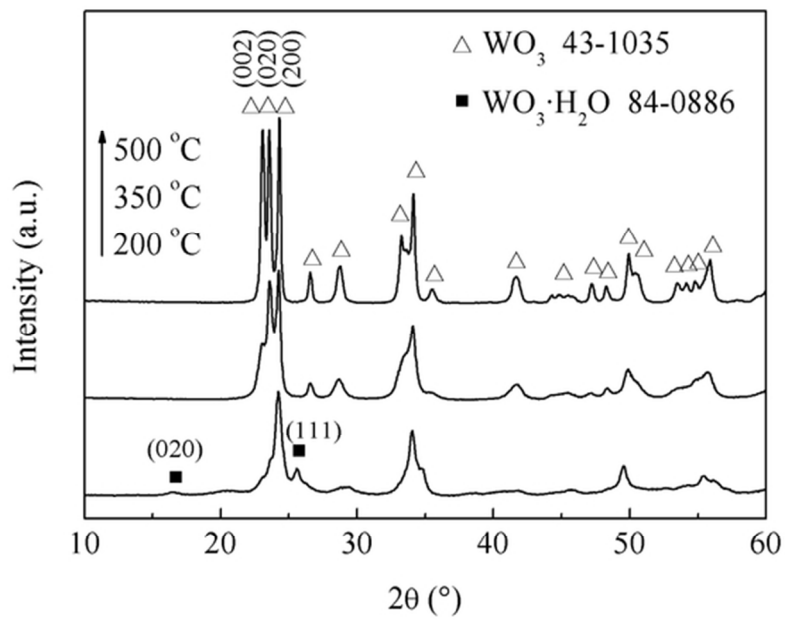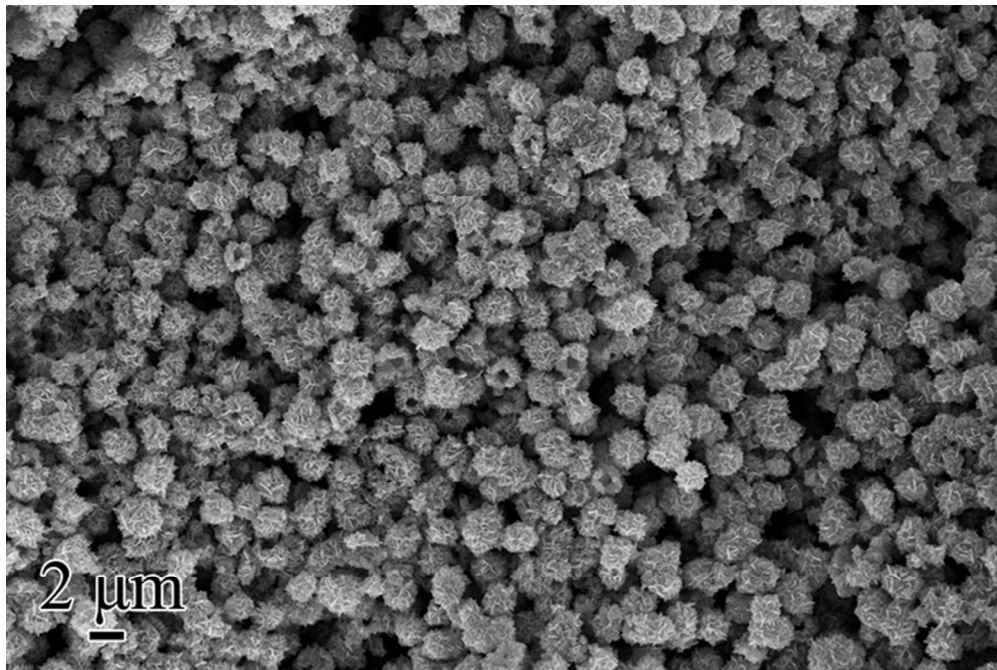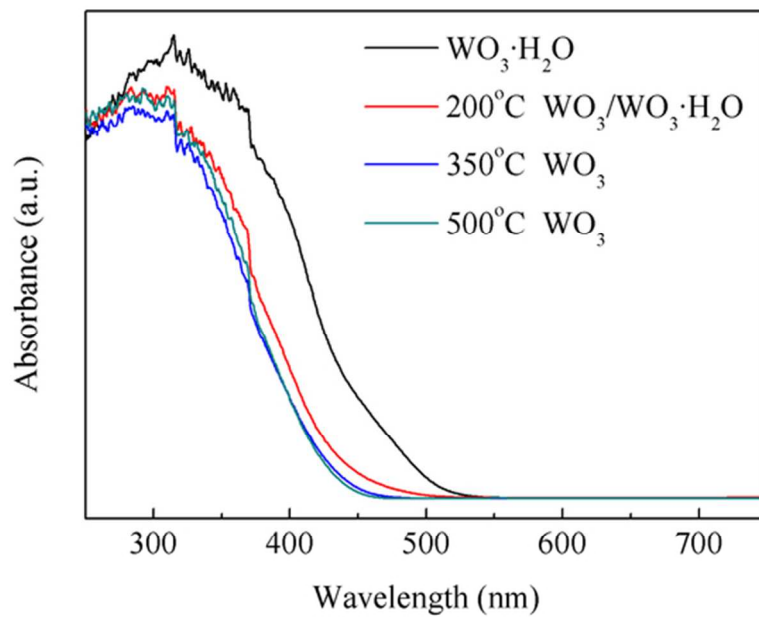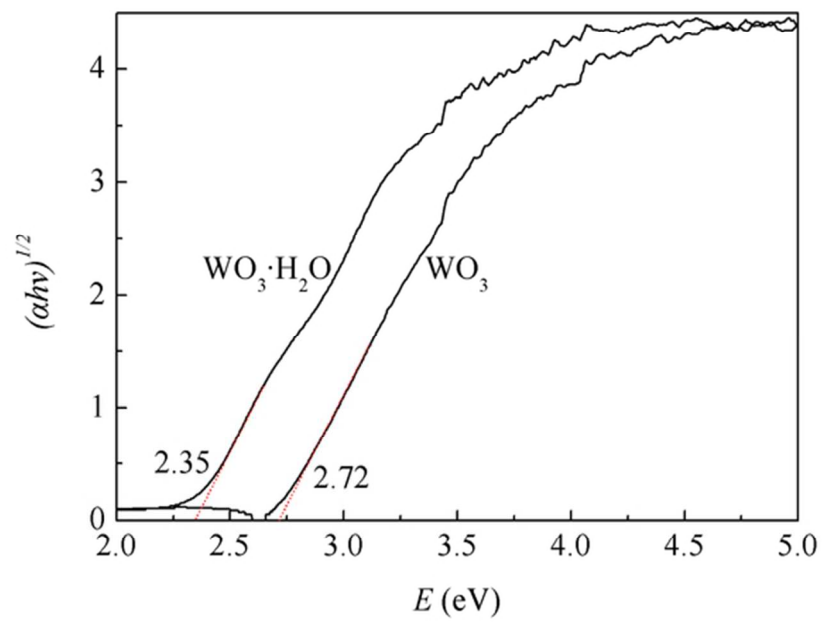
Figure 1
59x42mm (300 x 300 DPI)
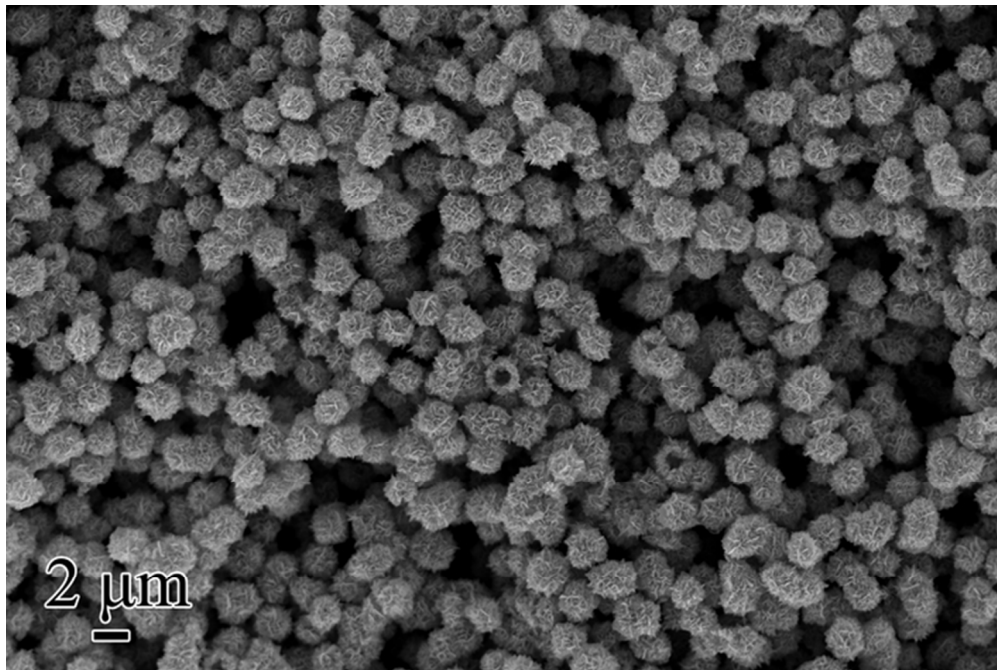
Figure 2a
59x39mm (300 x 300 DPI)
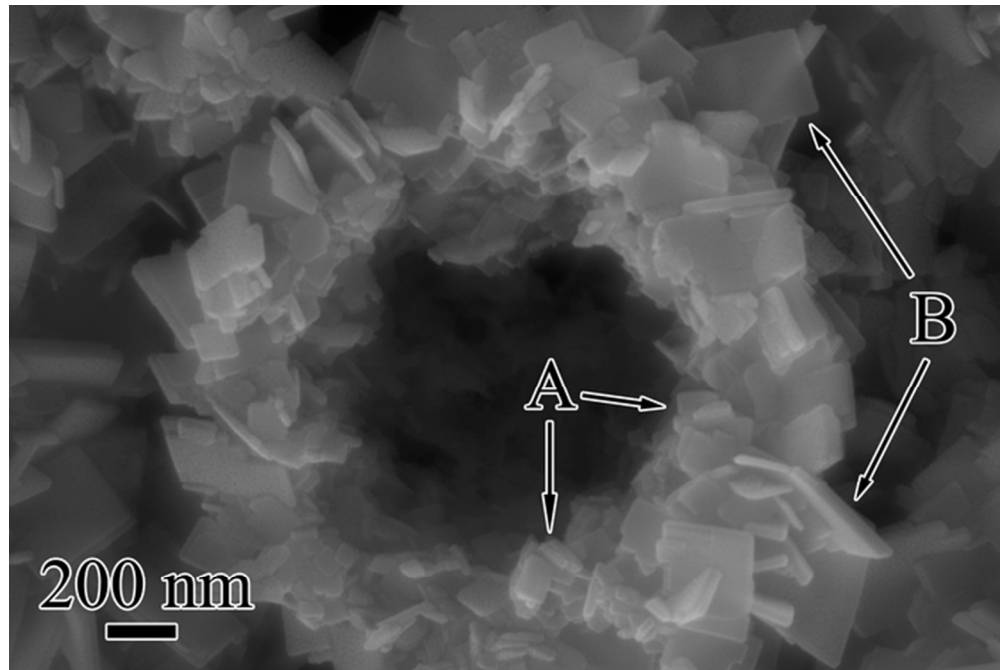
Figure 2b
59x39mm (300 x 300 DPI)
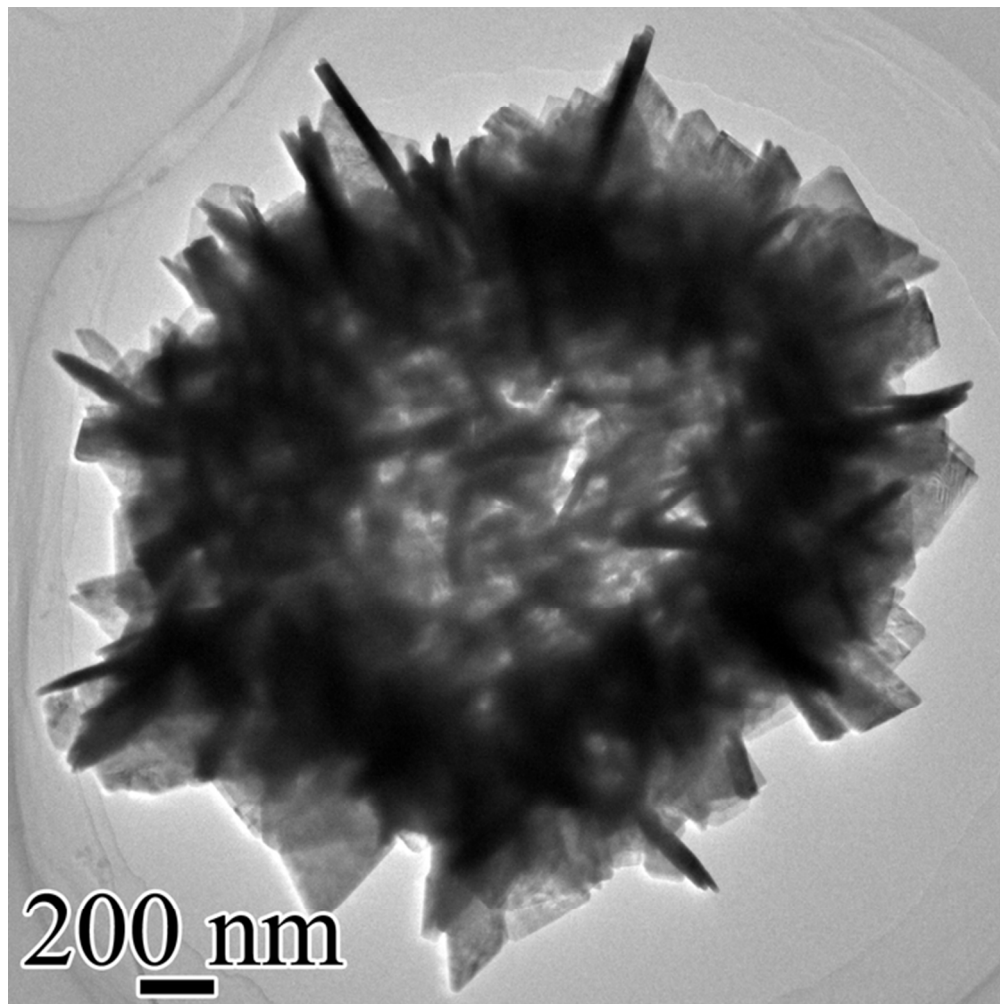
Figure 2c
59x59mm (300 x 300 DPI)

Figure 2d
59x59mm (300 x 300 DPI)

Figure 2e
59x59mm (300 x 300 DPI)

Figure 2f
59x59mm (300 x 300 DPI)

Figure 3a
59x59mm (300 x 300 DPI)

Figure 3b
59x59mm (300 x 300 DPI)

Figure 3c
59x59mm (300 x 300 DPI)

Figure 3d
59x59mm (300 x 300 DPI)

Figure 4
59x42mm (300 x 300 DPI)

Figure 5a
59x42mm (300 x 300 DPI)

Figure 5b
59x42mm (300 x 300 DPI)

Figure 5c
59x39mm (300 x 300 DPI)

Figure 6a
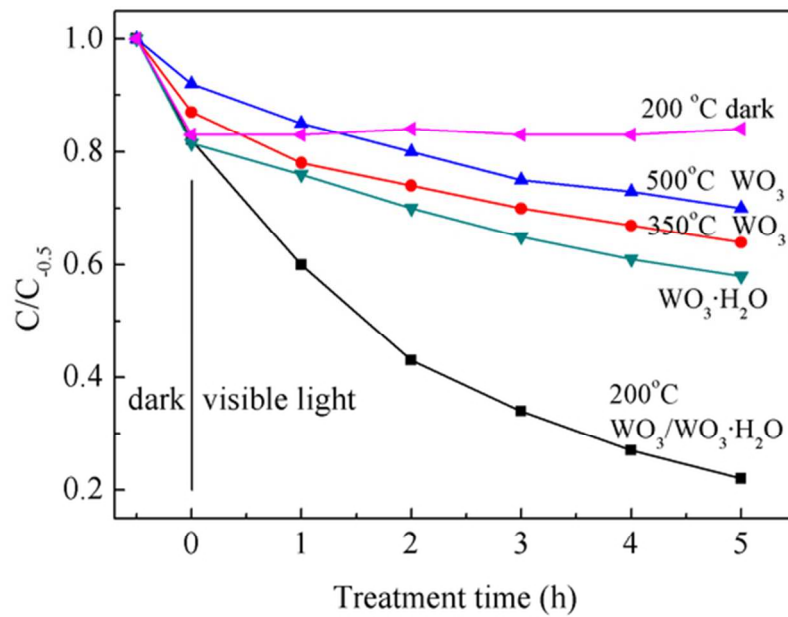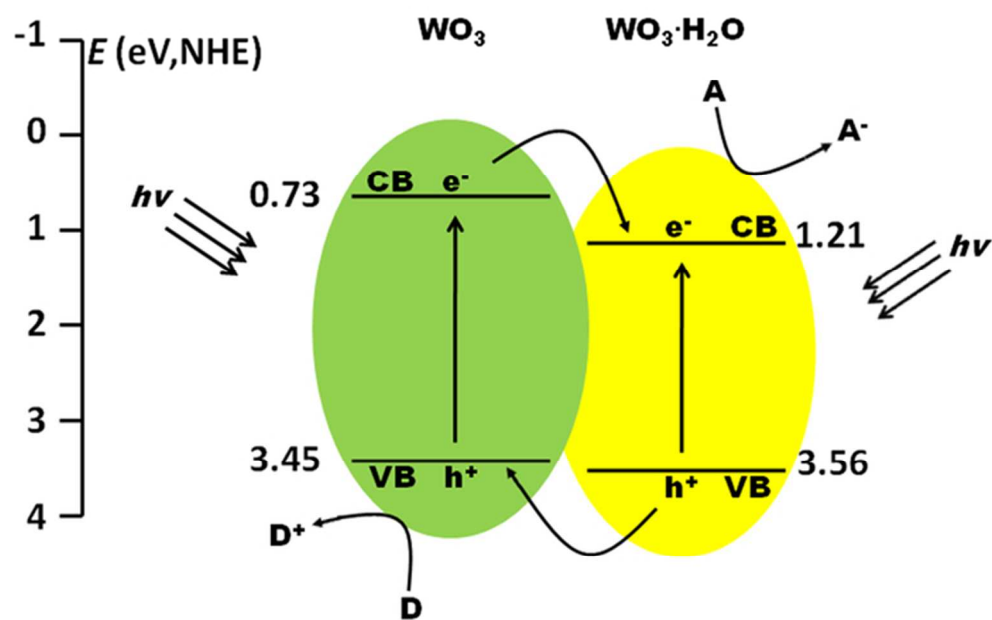59x42mm (300 x 300 DPI)

Figure 6b
59x42mm (300 x 300 DPI)

Figure 7
59x42mm (300 x 300 DPI)

Figure 8
59x39mm (300 x 300 DPI)